Irradiation-induced clustering in a high-Ni, high-Mn, low-Cu boiling water reactor pressure vessel weld after 28 full power years

Scripta Materialia 258 (2025) 116497

Contents lists available at ScienceDirect

Scripta Materialia

journal homepage: www.journals.elsevier.com/scripta-materialia

Irradiation-induced clustering in a high-Ni, high-Mn, low-Cu boiling water reactor pressure vessel weld after 28 full power years

David Mayweg [a,*], Kristina Lindgren [a,d], Pål Efsing [b,c], Mattias Thuvander [a]

[a] Chalmers University of Technology, Department of Physics, Göteborg SE-412 96, Sweden
[b] Department of Solid Mechanics, Royal Institute of Technology (KTH), Stockholm SE-100 44, Sweden
[c] Ringhals AB, Väröbacka SE-430 22, Sweden
[d] Now at RISE, Mölndal SE-431 53, Sweden

ARTICLE INFO

Keywords:
Irradiation-induced clustering
Atom probe tomography
Reactor pressure vessel steel
Boiling water reactor

ABSTRACT

High-Ni, high-Mn welds are the life-time determining components in reactor pressure vessels (RPVs) of Nordic reactors at desired operating times of pressurized water reactors (PWR) of 60 or even 80 years due to embrittlement that is caused by pronounced clustering of Ni, Mn and Si. To understand early stages of clustering we performed atom probe tomography (APT) measurements on an axial weld of the boiling water RPV from Barsebäck Unit 2 decommissioned after 28 years of operation. Contrary to our previous work on the same weldment, here we report observation of clustering. The cluster number densities vary significantly between individual APT measurements, which we attribute to variations in local Ni and Mn concentrations, a trend even seen within single grains. Based on comparison with high fluence samples containing more and larger clusters we propose that NiMnSi cluster formation and growth is an irradiation-induced continuous process without a relevant threshold dose.

Nuclear reactor pressure vessels (RPVs) are manufactured from ferritic low alloy steels [1]. Such steels exhibit a pronounced ductile to brittle transition (DBT) [2–4]. The DBT temperature (DBTT) is adversely affected by thermal ageing combined with neutron irradiation [5]. The ageing effects can be divided into non-hardening – mostly P segregation to grain boundaries (GBs) – and hardening effects, which are related to irradiation-induced defects from fast neutrons that facilitate diffusion and clustering or precipitation of solutes (Cu, Ni, Mn, Si, P) [3,4,6–8]. These mechanisms have been characterize by X-ray techniques [9,10], positron annihilation spectroscopy [11], and APT investigations [6, 12–23]. Early investigations of RPVs revealed that Cu plays a key role in embrittlement [2] due to formation of coherent Cu-rich precipitates [6, 14,15,24], which is accelerated by radiation enhanced diffusion [3]. The independent role of Ni in low-Cu (<0.05 at%) steels was only noticed some decades later [25,26] and it was proposed that NiMnSi clusters with negligible Cu fraction forming in such materials are subject to an incubation period [3,27]. Based on this assessment there is an ongoing debate with respect to the nature of these solute clusters in low-Cu steels, namely, if they are or can become separate phases at later stages, i.e., whether their formation is thermodynamically favored and accelerated by radiation enhanced diffusion [28,29] or they are stabilized by irradiation-induced point defects (vacancies and self-interstitial atoms) [30–32]. Following the model laid out by Castin et al. [31] we believe that, simply put, clusters in the low-Cu RPV welds that we are concerned with ([20] and this work) are mainly defect stabilized. The form via radiation induced segregation of solutes to point defects. Phase separation does not occur at relevant time scales (low-Cu, high-Ni material was the only alloy in a wide range of compositions where no evidence for G-phase formation was reported [10]).

Prediction of changes in the mechanical properties and assessment of the operative limits of RPVs is conducted in surveillance programs (e.g., [22,33]). In the case of the Nordic RPVs the welds are critical parts of the structure. At the time they were manufactured it was already known that Cu strongly enhances the irradiation embrittlement [24] and, hence, weld metal with low levels of Cu [33] and some 1.5 wt% Ni and Mn was used. For the RPVs of Ringhals Unit 3 and 4 an R&D program to support long term operation has been undertaken [17,18,20,21,34]. To understand the full microstructure evolution starting at low damage levels materials were harvested from the decommissioned boiling water reactor (BWR) Barsebäck Unit 2 RPV [35]. This material has been subjected to mechanical and microstructural characterization [36,37] and atom probe tomography (APT) [38]. The current study is an extension of

* Corresponding author.
E-mail addresses: david.mayweg@chalmers.se, david.mayweg@gmail.com (D. Mayweg).

https://doi.org/10.1016/j.scriptamat.2024.116497
Received 26 October 2024; Received in revised form 5 December 2024; Accepted 6 December 2024
Available online 12 December 2024

Table 1
Chemical composition determined by optical emission spectroscopy (from [37]).

	Ni	Mn	Si	Mo	C	Cu	Cr	Co	P	Al	S	Fe
at%	1.58	1.45	0.32	0.26	0.25	0.06	0.03	0.02	0.02	0.004	0.009	bal.
wt%	1.66	1.43	0.16	0.44	0.054	0.07	0.03	0.02	0.01	0.02	0.005	bal.

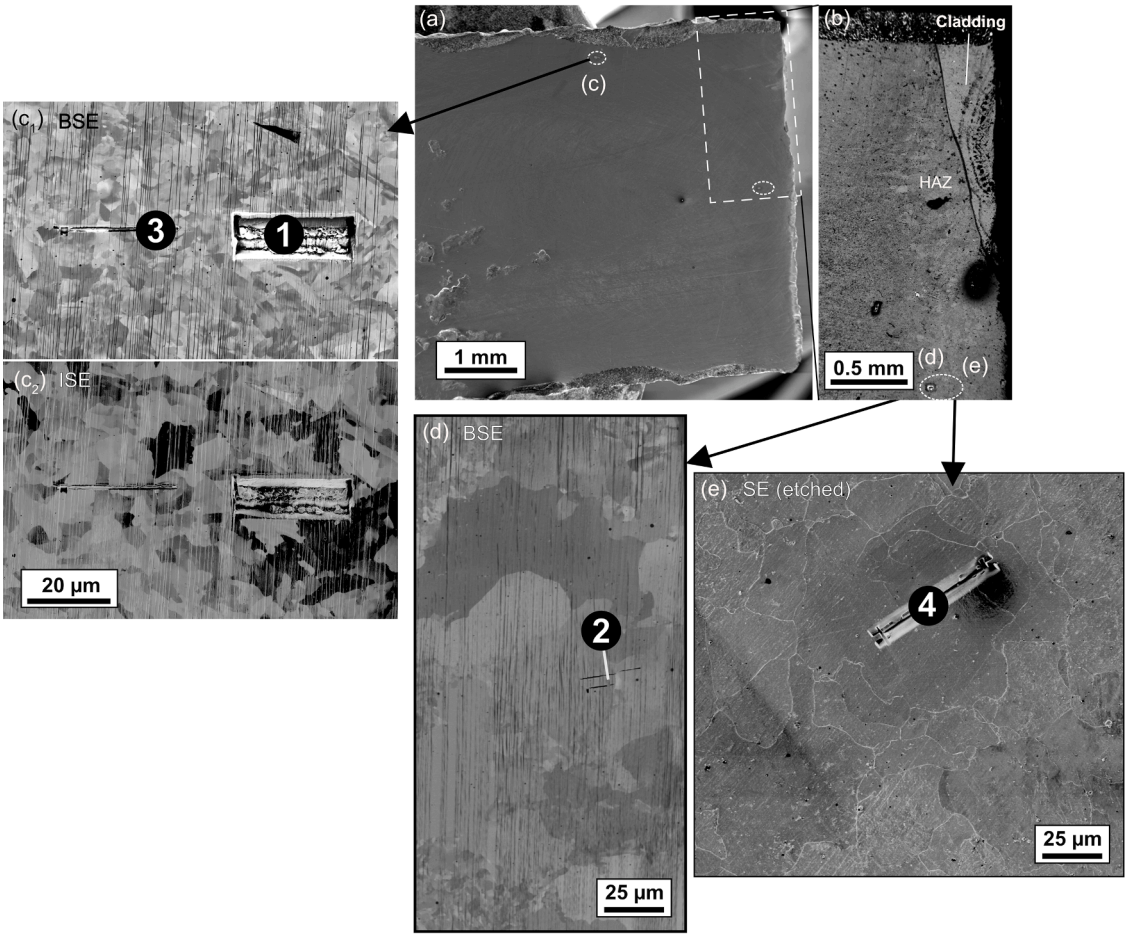

Fig. 1. Electron images of a sample from an axial weld of the Barsebäck 2 RPV weld close to the cladding. (a) Overview secondary electron (SE) image, (b) backscatter electron (BSE) image highlighting the cladding and the HAZ. (c_1) and (c_2) are BSE and ion-induced secondary electron images (ISE) of APT lift-out locations from the normal weld microstructure (position 1 from [38]). (d) and (e) are BSE and SE images of the lift-out location in the HAZ adjacent to the cladding.

the work in [38] and features more APT measurements to understand the early-in-life behavior of NiMnSi clusters formed during reactor operation.

We investigated an axial beltline weld (bulk composition, see Table 1) from the Barsebäck 2 RPV reaching a nominal fast neutron fluence of 7.9×10^{21} n/m^2 (28 full power years). The DBTT was not affected [37] (Yuya et al. [39] reported a DBTT shift of +26 °C for a BWR RPV with a fluence of 1.5×10^{22} n/m^2 containing 1.48 wt% Mn, 0.56 wt % Ni and 0.09 wt% Cu). APT specimen preparation was performed using an FEI Versa3D focused ion beam using standard procedures [40] (final annular milling: nominal 30 or 50 pA at 30 kV with mask inner diameter 100 nm, final cleaning at 2 kV and 28 pA for 30 s).

APT experiments were conducted in a Cameca LEAP 6000XR (detection efficiency 52 %, laser wavelength 257.5 nm). Experimental parameters are provided in a table in the supplementary material. In voltage pulsing APT the number of collected ions often was relatively small (typically 1–3 $\times$ 10^6 ions) so we additionally used laser pulsing APT, which is less well-suited for characterizing cluster size and

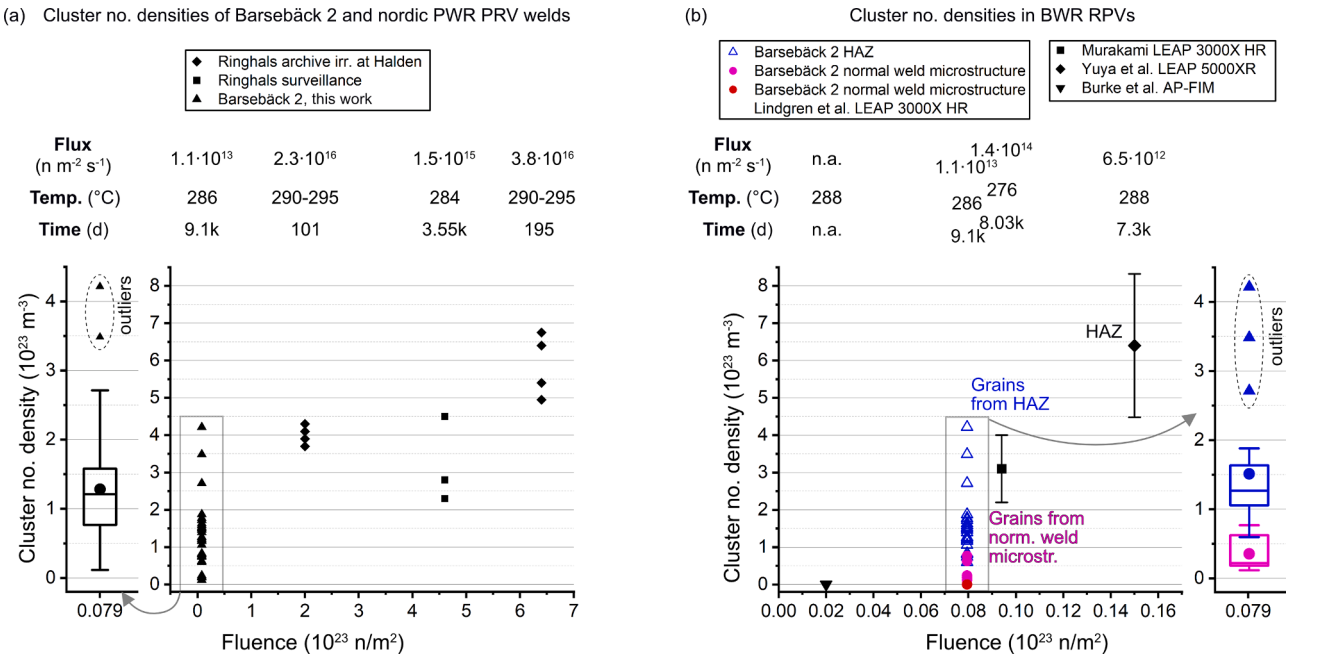

Fig. 2. Cluster number density vs. fast neutron fluence (> 1 MeV), with flux, irradiation temperature and time given above the plots. In (a) the data obtained in this work (that are additionally represented as a box plot) are compared to high fluence data from Nordic (high-Ni, high-Mn, low-Cu) RPV steel from [20]. In (b) our data (colored, see text) are presented in comparison to low fluence literature values from BWR RPVs [14,38,39,49]. Again, the data from the present work are additionally represented in box plots. Note that Burke et al. [14] used AP-FIM and did not detect any clusters at all, likely due to the small captured volumes.

Table 2
Statistics of the cluster number densities (10^{23} clusters/m^3) from our APT experiments.

	All data from this work combined	Normal weld microstructure	Heat-affected zone (HAZ)	Yuya [39] (HAZ)	Murakami [49]
N (no. of APT datasets)	31	6	25	41	–
Mean	1.3	0.4	1.5	6.4	3.1
Standard deviation	0.9	0.3	0.8	1.6	0.9
Median	1.2	0.2	1.3	–	–
Maximum	4.2	0.8	4.2	–	–
Minimum	0.2	0.2	0.6	–	–

composition as it is leading to significant surface diffusion of Si, P and Cu [41]. But since laser pulsing allows for the collection of much larger datasets (> 10^7 ions) we used it to capture larger volumes increasing the confidence in the cluster number density determination. All datasets were crystallographically calibrated [42,43]. Compositions were calculated using the built-in peak decomposition in AP Suite 6.3. In voltage pulsing Mn and Cu are systematically underestimated [41] (see supplementary material, Appendix A). Cluster analysis was performed using the version of the maximum separation method [44] implemented in AP Suite 6.3. For voltage pulsing datasets we included Ni, Mn and Si

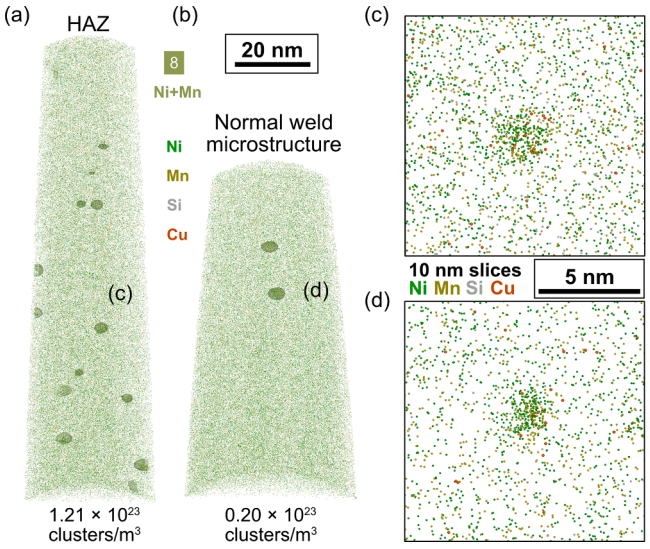

Fig. 3. (a) and (b) are 3D atom maps from APT reconstructions displaying Ni, Mn, Si and Cu from the HAZ (50 K, 15 pJ) and the normal weld microstructure (50 K, 20 pJ), respectively. 6 at% Ni+Mn ICSs highlight larger clusters. The views in (c) and (d) depict 10 nm slices including a single cluster from (a) and (b).

Table 3
Comparison of compositions of the specimens in Fig. 3 (50 K base temperature and 20 and 15 pJ LPE).

	Normal weld microstructure		HAZ	
Clusters/ m^3	0.20×10^{23}		1.21×10^{23}	
	Composition (at%)			
	Full dataset	6 at% Ni+Mn ICS removed	Full dataset	6 at% Ni+Mn ICS removed
Ni	1.40	1.39	1.47	1.44
Mn	1.19	1.18	1.37	1.35
Si	0.20	0.20	0.29	0.28
Cu	0.04	0.04	0.04	0.04

ions, for laser pulsing datasets only Ni and Mn were used. P and Cu are only present in small amounts and were therefore not included in the cluster search. For every dataset we performed a sweep of the maximum separation distance (d_{max}) and chose this parameter from the plateau region between 0.4 and 0.55 nm (see Figure S1). If no clear plateau was present, we chose the value with the lowest slope between 0.4 and 0.6 nm. Clusters with 25 or more detected solute atoms were considered for analysis. The cluster numbers obtained for each dataset agree well with isoconcentration-surface-(ICS)-based cluster identification (typically 10–20 % difference, see Figure S2). Radial concentration profiles were created based on the cluster dimensions of the identified solutes in AP Suite. Most of the clusters found in the here presented work have radii smaller than ~ 1 nm (~ 350 atoms) for which compositions cannot be reliably determined by APT [45]. Since large clusters (> 3000 atoms) from comparable high fluence material [20] did contain Fe, we included it in the cluster composition analysis although it is most likely significantly overestimated. Because we cannot quantify the lateral resolution and the evaporation field differences we are not able to determine the real Fe fraction inside clusters [46].

Fig. 1 comprises electron images of the bulk specimen from which the lift-outs for APT analyses were taken: (a) is an overview marking the approximate positions of the lift-outs by dashed ellipses and (b) is a magnified view of the dashed rectangle in (a) highlighting the cladding in the upper right and the coarse-grained heat affected zone (HAZ). The grain morphology is shown in (c) – (e): The same region from the normal weld microstructure is depicted in (c_1) and (c_2) as a backscatter electron and an ion-induced secondary electron image, respectively, both showing the typical weld morphology. (d) shows the transition region, where weld morphology is visible in direct vicinity of grains that extend over more than 100 μm. Finally, (e) is depicting a region in the HAZ where only coarse grains are present.

Fig. 2(a) is a plot comparing cluster number densities obtained in the present work with high fluence (high flux) data from Nordic RPV welds: a surveillance specimen from Ringhals Unit 4 and its archive material irradiated in the Halden research reactor [20] (note that the cluster sizes are significantly different). The data from the present work are additionally presented as a box plot. Fig. 2(b) is a comparison of the present results with low fluence (low flux) literature data (note that cluster analysis results strongly depend on the parameter choice [47,48]) from BWRs including earlier work from the same weldment where no clusters of any kind were found in 10 needle specimens ([38] see lift-out location 1 in Figure 1 (c)). The data from the Barsebäck 2 RPV weld are represented in magenta for the normal weld microstructure, blue for the HAZ and red (from [38]), while the literature values are shown in black. The box plots of the data from this work provide a better visualization of the number density statistics that are provided in Table 2 alongside literature values for comparison (note the different Cu levels: Murakami [49] 0.24 wt%; Yuya et al. [39] 0.09 wt% Cu).

The plots in Fig. 2 clearly show that comparatively higher cluster number densities are found in coarse grains of the HAZ. Also noteworthy is the large scatter with the highest values on the level of that seen in the Ringhals 4 material.

Fig. 3 allows for visual comparison of two APT specimens from the HAZ and the normal weld microstructure (coarse- and fine-grained regions), respectively. Clusters are scarce but recognizable by visual inspection. The reconstruction depicted in Fig. 3(a) and (c) is from lift-out position 2 (Fig. 1(d)), while that shown in Fig. 3(b) and (d) is from lift-out position 3 (Fig. 1(c)). The cluster number density of the dataset from HAZ is six times larger than that of the fine-grained region, which is associated with an 0.25 at% higher Ni+Mn fraction as listed in Table 3.

The table includes measured fractions (clusters included vs. removed) of Ni and Mn in the two APT specimens in Fig. 3. Similar experimental parameters ensure comparability. Because of the low volume fraction of the clusters the difference is not due to the presence of clusters but the larger total concentration of these elements.

Fig. 4(a) shows an secondary electron (SE) image of the HAZ with a very large grain (Grain 1). We performed a lift-out targeting a total of three grains, including a GB and a region spanning roughly 20 μm inside Grain 1. The positions of the individual specimens are marked by color-coded circles. Figure 4 (b) depicts a plot of cluster number density over the Ni+Mn fraction for the individual APT measurements. Only laser pulsing datasets were included in the linear fit ($R^2 = 0.74$, $p = 0.002$) because of underestimation of Mn in voltage pulsing (arrows indicate their positions 'corrected' by 0.25 at%). The GB was captured in one measurement and a reconstruction of this dataset is presented in Figure 4 (c). There appears to be a cluster denuded zone with a width of approximately 50 nm next to the GB; the Ni, Mn and Si fractions are nearly identical in this region compared to the volume in which clusters are present. This observation can be rationalized by GBs acting as sinks for point defects [50,51]. Assuming their presence is a precondition for cluster formation [31] the absence of clusters indicates a relevant reduction in the number of point defects. The plot in Figure 4 (b) shows that cluster number densities are varying by a factor as large as five with the fraction of Ni and Mn even within a single grain (Grain 1). Figure 4 (d) shows two plots of the Ni- and Mn-fraction (balance almost exclusively Fe) in the clusters from measurements #6 and #8 highlighted in Figure 4 (b) by a triangle and a diamond symbol, respectively. Cluster size (number of atoms per cluster) and composition show similar distributions.

This assessment is confirmed quantitatively in Table 4. The 0.5 at% larger Ni+Mn fraction is associated with a five times higher cluster number density, while average cluster composition and number of atoms per cluster are similar. A possible conclusion is that cluster formation is more enhanced by the larger solute fractions than the degree of acceleration in growth of individual clusters.

From an assessment of all laser pulsing datasets (Table 5, see respective plots in Figure S3) a significant correlation of cluster number

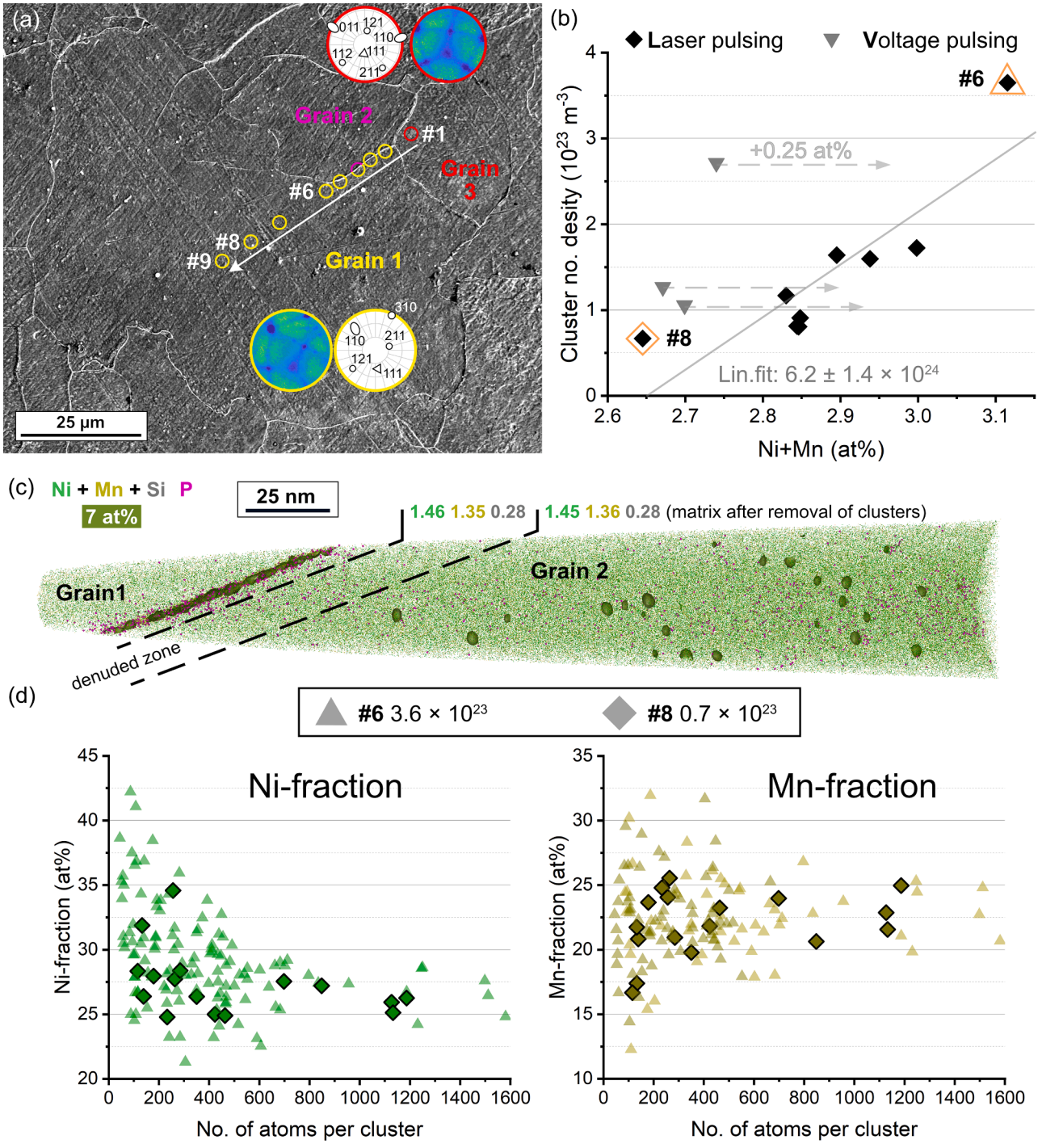

Fig. 4. Clustering in the HAZ near the cladding. (a) is an SE image after etching with 5 % Nital; the positions of the individual APT specimens are marked by circles and color-coded for grains 1, 2, and 3 (identified based on their crystallographic orientation, see insets obtained with code from [43]). (b) shows plots of cluster number density vs. the Ni+Mn fraction (fitting the data from laser pulsing datasets yields $R^2 = 0.74$, $p = 0.003$). The open triangles are the voltage pulsing datasets with (c) a reconstruction from lift-out position 4 (magenta circle segment) including a GB, showing a potentially cluster denuded zone (the composition of the volumes separated by dashed lines ins given in the same color coding as the ions). (d) comparison of Ni and Mn fraction in the clusters of APT specimens #6 and #8 from Grain 1 (marked extreme cases in (b) by a triangle and a diamond).

Table 4
Cluster statistics of the two APT datasets shown in Fig. 4(d) from specimens #6 and #8. Cluster analysis parameters: $d_{max} = 0.42$ nm, $N_{min} = 25$, $L = e = 0.25$ nm). The value given after the ± sign is the standard deviation.

	Specimen	
	#6	#8
No. of clusters	123	18
Cluster no. density (10^{23} m^{-3})	3.6	0.7
Volume (10^{-23} m^3)	33.7	26.9
No. of ions per cluster incl. Fe	271 ± 177	234 ± 196
No. ions per cluster excl. Fe	140 ± 91	120 ± 100
Ni in clusters (at%)	29.2 ± 3.9	27.0 ± 3.9
Mn in clusters (at%)	22.5 ± 3.2	22.8 ± 4.2
Ni in full spectrum (at%)	1.62	1.33
Mn in full spectrum (at%)	1.50	1.31

Table 5
Results from linear regression of the composition and cluster number density data points from all laser pulsing datasets from this work.

	Ni	Mn	Si	Cu	P	C
Slope (10^{24} clusters m^{-3}/at %)	1.08 ±0.15	1.13 ±0.17	2.73 ±0.93	3.21 ±2.36	10.79 ±6.25	−0.28 ±1.07
R^2	0.71	0.68	0.29	0.08	0.13	0.003
p	4E-7	1.2E-6	> 0.01	0.19	0.10	0.80

density and solute fraction was confirmed for Ni, Mn, Si but not for Cu, P and C.

Fig. 5 is a comparison of solute clustering in the Barsebäck 2 (B2) RPV weld and a Ringhals 4 (R4) surveillance sample of nominally 58 times higher fluence [20]. The two specimens were measured with similar APT parameters (70/50 K, 20 % pulse fraction, detection rate 0.5 %, LEAP 6000XR and LEAP 3000X HR). The overall difference in cluster size and their different compositions are highlighted by the atom maps in Fig. 5(a) and (b). The 6 at% (Ni+Mn+Si) ICSs in Figure 5 (a) highlight the difference in cluster volume and number density. The clusters in the two materials are however more similar than they visually appear as Figure 5 (c) demonstrates (see also Figure S4). It comprises plots of radial concentration profiles for Ni and Mn where clusters are divided in size groups (calculated including Fe, clusters > 2000 atoms/cluster are excluded since those are not present in the B2 specimen; they are depicted in Figure S5). While the R4 clusters exhibit slightly higher concentrations near the center (see also Figure S6), the profiles for the two specimens are strikingly similar despite the significant difference in fluence. Table 6 includes a comparison of the matrix fractions of Ni and Mn in the specimens shown in Fig. 5. It is apparent that in both cases clustering leads to depletion of the matrix although due to the small volume fraction of the clusters this is not very pronounced in the B2 material. What is interesting to note is that Ni and Mn fractions are lower in the matrix of the R4 specimen, i.e., the continued irradiation leads to successive removal of Ni and Mn from the matrix.

According to the model in [31] nuclei (as small as two solutes segregated to a point defect cluster) continuously form and grow by addition of further solute/point defect pairs; dissolution by emission of vacancy solute pairs can also occur. Therefore, clusters are expected to have different size as function of flux, time, temperature and (local) composition. The assumption that irradiation-induced clustering took place in the here presented materials is supported by the lack of comparable NiMnSi clusters after purely thermal annealing of similar welds [52]. There, exclusively precipitates with Cu-rich cores and NiMnSi-shells were found near dislocations. This finding is particularly meaningful due to the comparatively large amount of data that was collected from 19 electropolished wire specimens. Additional support for this interpretation is a post irradiation annealing (PIA) study of Nordic RPV welds by Lindgren et al. [53] that indicates low stability of NiMnSi clusters found in these materials: while they disappeared after 24 h at 410 °C, Cu-rich clusters near dislocations similar to those in the purely thermally annealed weld in [52] remained. Even as this line of reasoning appears to be consistent, there remains room for debate. It is for example not clear why the clusters shown in Fig. 4(d) have similar (measured) compositions although the local Ni+Mn fraction varies by 0.5 at%. These differences in matrix composition should be reflected in the cluster composition [32]. In addition, there is evidence for similar low-Cu, high-Ni model alloys indicating a much higher stability of NiMnSi clusters. For example, PIA studies by Almirall et al. [29,54] showed that some large clusters persisted after up to more than one year at 425 °C. Based on the available information in [20,29,52–54] we do not see any obvious explanation for this discrepancy.

In conclusion we would like to summarize the findings from our APT results obtained from a low fluence, low flux BWR RPV weld as follows.

Cluster number densities between individual APT measurements vary by a factor of up to 36 between the smallest and the highest value. The significant variation in cluster number density across many APT specimens is correlated with – and likely caused by – the local Ni and Mn concentrations as was shown to be the case even within a single grain (Fig. 4 and Figure S3). One APT measurement capturing a GB can be construed as showing a cluster denuded zone, which might be explained by the GB constituting a sink for point defects.

The key finding from our work is that there appears to be no fundamental difference between clusters in the low fluence Barsebäck 2 and the high fluence Ringhals surveillance weld material. We have shown that NiMnSi clustering in *Nordic RPV steel weldments* takes place already at low fluence. These clusters are similar to those in high fluence weldments and differ from others found after thermal annealing [52, 55]. We therefore propose that their existence comes about by a continuous process of defect-mediated cluster formation that is accompanied by the growth of already existing clusters.

A final note on our previous study [38]: We do not have a good explanation why we did not find clusters in the previous APT experiments. The matrix of specimens from the present work shows slightly higher probability of Ni-Ni (Ni-Mn, Ni-Si, Ni-Cu) neighborhood in a very similar manner as shown in [38], indicating early clustering that eludes recognition due to limitations of the technique [48]. In conclusion we can hence only emphasize again, that APT studies are prone to insufficient sample sizes limiting the statistical power.

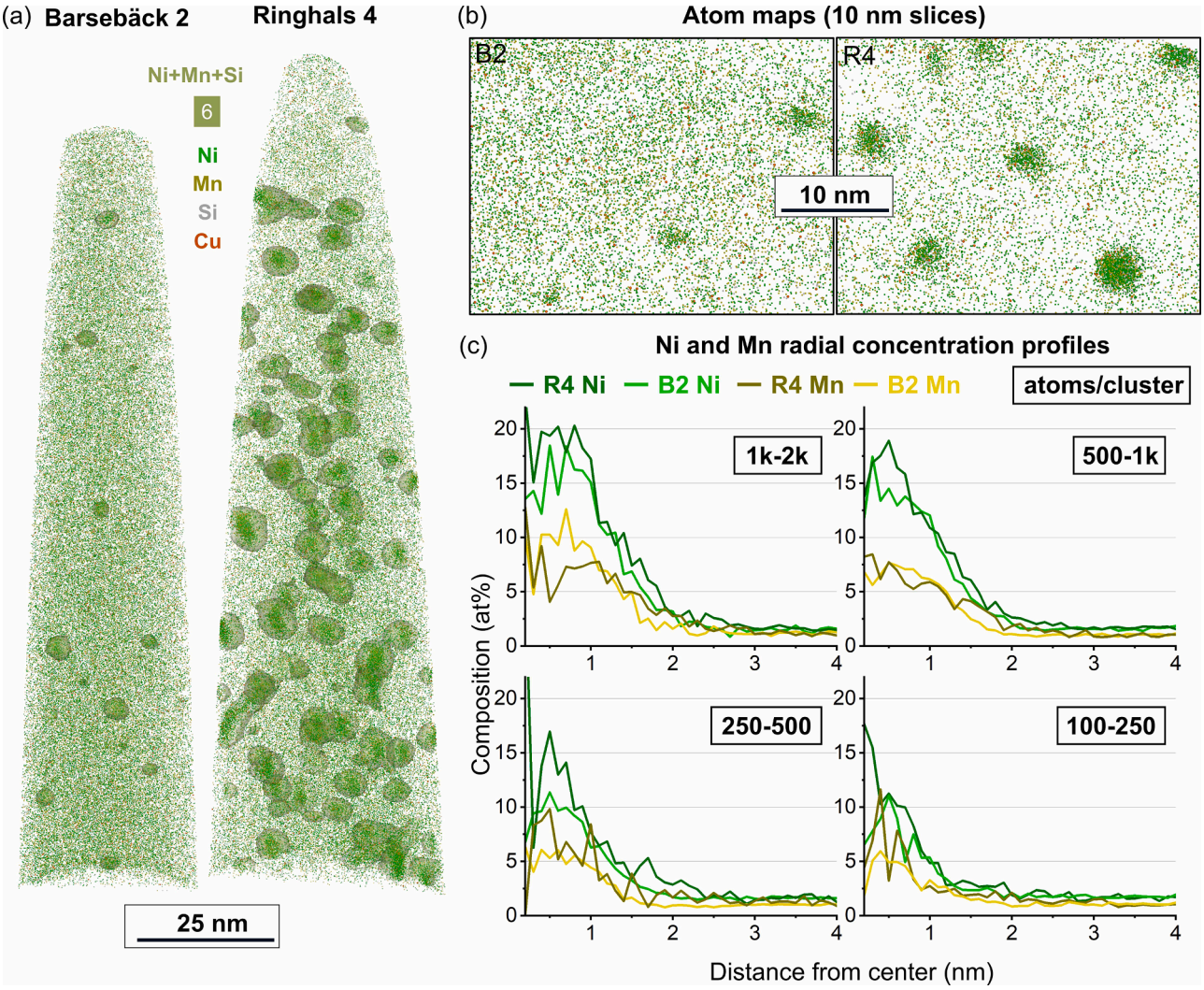

Fig. 5. Comparison of APT data from Barsebäck 2 (B2) RPV (70 K, 20 % PF) and from Ringhals 4 surveillance material (R4) from Lindgren et al. [20] (50 K, 20 % PF). (a) Atom maps of voltage pulsing datasets with clusters highlighted by 6 at% Ni+Mn+Si ICSs. Note that this value does not appear to be a well-suited descriptor for the R4 specimen, but was chosen for the purpose of comparison. (b) Atom maps of 10 nm thick volumes highlighting the appearance of individual clusters. (c) Radial concentration profiles for Ni and Mn cluster size classes (clusters > 2000 atoms were only present in the R4 specimen and are not included here; plots are available in the supplementary material).

Table 6
Volume fraction of clusters and composition (in at%) of the matrix after removal of the clusters from the datasets in Fig. 5.

	B2	R4
Volume fraction (%)	0.15	2.11
Total Ni	1.37	1.73
Ni matrix	1.35	1.21
Total Mn	1.13	1.27
Mn matrix	1.11	1.00

CRediT authorship contribution statement

David Mayweg: Writing – review & editing, Writing – original draft, Visualization, Methodology, Investigation, Formal analysis, Conceptualization. **Kristina Lindgren:** Writing – review & editing, Investigation, Funding acquisition. **Pål Efsing:** Writing – review & editing, Writing – original draft, Funding acquisition, Conceptualization. **Mattias Thuvander:** Writing – review & editing, Supervision, Funding acquisition, Conceptualization.

Declaration of competing interest

The authors declare that they have no known competing financial interests or personal relationships that could have appeared to influence the work reported in this paper.

Acknowledgments

This research was funded by the Nordic Nuclear Safety (NKS) projects BREDA and REPoUSSES, and by the Euratom research and training programme 2019-2020; European Database for Multiscale Modelling of Radiation Damage (ENTENTE), Grant agreement No. 900018. The authors want to thank Jenny Roudén and Johan Blomström (Ringhals AB) who provided valuable information about the specimen history. DM is thankful for fruitful discussions with Milan Konstantinović and Nicolas Castin. This work was carried out at Chalmers Materials Analysis Laboratory (CMAL).

Supplementary materials

Supplementary material associated with this article can be found, in

the online version, at doi:10.1016/j.scriptamat.2024.116497.

References

[1] T. Allen, J. Busby, M. Meyer, D. Petti, Materials challenges for nuclear systems, Mater. Today 13 (12) (2010) 14–23.
[2] L.E. Steele, Status of USA Nuclear Reactor Pressure Vessel Surveillance for Radiation Effects, ASTM International, West Conshohocken, PA, 1983.
[3] G.R. Odette, G.E. Lucas, Recent progress in understanding reactor pressure vessel steel embrittlement, Radiat. Effects Defects Solids 144 (1–4) (1998) 189–231.
[4] K. Fukuya, Current understanding of radiation-induced degradation in light water reactor structural materials, J. Nucl. Sci. Technol. 50 (3) (2013) 213–254.
[5] Integrity of reactor pressure vessels in nuclear power plants: assessment of irradiation embrittlement effects in reactor pressure vessel steels, International Atomic Energy Agency, Vienna, 2009.
[6] M.K. Miller, M.G. Burke, An atom probe field ion microscopy study of neutron-irradiated pressure vessel steels, J. Nucl. Mater. 195 (1) (1992) 68–82.
[7] W.J. Phythian, C.A. English, Microstructural evolution in reactor pressure vessel steels, J. Nucl. Mater. 205 (1993) 162–177.
[8] J.T. Buswell, W.J. Phythian, R.J. McElroy, S. Dumbill, P.H.N. Ray, J. Mace, R. N. Sinclair, Irradiation-induced microstructural changes, and hardening mechanisms, in model PWR reactor pressure vessel steels, J. Nucl. Mater. 225 (1995) 196–214.
[9] F. Bergner, M. Lambrecht, A. Ulbricht, A. Almazouzi, Comparative small-angle neutron scattering study of neutron-irradiated Fe, Fe-based alloys and a pressure vessel steel, J. Nucl. Mater. 399 (2–3) (2010) 129–136.
[10] D.J. Sprouster, J. Sinsheimer, E. Dooryhee, S.K. Ghose, P. Wells, T. Stan, N. Almirall, G.R. Odette, L.E. Ecker, Structural characterization of nanoscale intermetallic precipitates in highly neutron irradiated reactor pressure vessel steels, Scr. Mater. 113 (2016) 18–22.
[11] M.J. Konstantinović, I. Uytdenhouwen, G. Bonny, N. Castin, L. Malerba, P. Efsing, Radiation induced solute clustering in high-Ni reactor pressure vessel steel, Acta Mater. 179 (2019) 183–189.
[12] M.K. Miller, K.F. Russell, Embrittlement of RPV steels: an atom probe tomography perspective, J. Nucl. Mater. 371 (1) (2007) 145–160.
[13] M.K. Miller, M.A. Sokolov, R.K. Nanstad, K.F. Russell, APT characterization of high nickel RPV steels, J. Nucl. Mater. 351 (1) (2006) 187–196.
[14] M.G. Burke, S.P. Grant, M.K. Miller, APFIM investigations of solute clusterig and precipitation in irradiated RPV steels, in: 4th International Conference in Nuclear Power Systems - Water Reactors, Jekyll Island, GA, USA, 1989.
[15] M.K. Miller, M.G. Hetherington, M.G. Burke, Atom probe field-ion microscopy: a technique for microstructural characterization of irradiated materials on the atomic scale, Metall. Trans. A 20 (12) (1989) 2651–2661.
[16] E. Meslin, B. Radiguet, P. Pareige, A. Barbu, Kinetic of solute clustering in neutron irradiated ferritic model alloys and a French pressure vessel steel investigated by atom probe tomography, J. Nucl. Mater. 399 (2) (2010) 137–145.
[17] M.K. Miller, K.A. Powers, R.K. Nanstad, P. Efsing, Atom probe tomography characterizations of high nickel, low copper surveillance RPV welds irradiated to high fluences, J. Nucl. Mater. 437 (1) (2013) 107–115.
[18] P.D. Styman, J.M. Hyde, D. Parfitt, K. Wilford, M.G. Burke, C.A. English, P. Efsing, Post-irradiation annealing of Ni–Mn–Si-enriched clusters in a neutron-irradiated RPV steel weld using Atom Probe Tomography, J. Nucl. Mater. 459 (2015) 127–134.
[19] P.D. Edmondson, M.K. Miller, K.A. Powers, R.K. Nanstad, Atom probe tomography characterization of neutron irradiated surveillance samples from the R. E. Ginna reactor pressure vessel, J. Nucl. Mater. 470 (2016) 147–154.
[20] K. Lindgren, M. Boåsen, K. Stiller, P. Efsing, M. Thuvander, Evolution of precipitation in reactor pressure vessel steel welds under neutron irradiation, J. Nucl. Mater. 488 (2017) 222–230.
[21] K. Lindgren, K. Stiller, P. Efsing, M. Thuvander, On the analysis of clustering in an irradiated low alloy reactor pressure vessel steel weld, Microsc. Microanal.: Off. J. Microsc. Soc. America, Microbeam Anal. Soc., Microsc. Soc. Canada 23 (2) (2017) 376–384.
[22] B.M. Jenkins, J.O. Douglas, N. Almirall, N. Riddle, P.A.J. Bagot, J.M. Hyde, G. R. Odette, M.P. Moody, The effect of composition variations on the response of steels subjected to high fluence neutron irradiation, Materialia (Oxf) 11 (2020).
[23] N. Almirall, P.B. Wells, T. Yamamoto, K. Wilford, T. Williams, N. Riddle, G. R. Odette, Precipitation and hardening in irradiated low alloy steels with a wide range of Ni and Mn compositions, Acta Mater. 179 (2019) 119–128.
[24] G.R. Odette, On the dominant mechanism of irradiation embrittlement of reactor pressure vessel steels, Scr. Metall. 17 (10) (1983) 1183–1188.
[25] M.M. Ghoneim, F.H. Hammad, Pressure vessel steels: influence of chemical composition on irradiation sensitivity, Int. J. Pressure Vessels Piping 74 (3) (1997) 189–198.
[26] C. Guionnet, B. Houssin, D. Brasseur, A. Lefort, D. Gros, R. Perdreau, Radiation embrittlement of PWR reactor vessel weld metals: nickel and copper synergism effects, in: J.S. Perrin (Ed.), Effects of Radiation on Materials, ASTM International, West Conshohocken, PA, pp. 392–411.
[27] G.R. Odette, T. Yamamoto, T.J. Williams, R.K. Nanstad, C.A. English, On the history and status of reactor pressure vessel steel ductile to brittle transition temperature shift prediction models, J. Nucl. Mater. 526 (2019).
[28] H. Ke, P. Wells, P.D. Edmondson, N. Almirall, L. Barnard, G.R. Odette, D. Morgan, Thermodynamic and kinetic modeling of Mn-Ni-Si precipitates in low-Cu reactor pressure vessel steels, Acta Mater. 138 (2017) 10–26.
[29] N. Almirall, P.B. Wells, H. Ke, P. Edmondson, D. Morgan, T. Yamamoto, G. R. Odette, On the elevated temperature thermal stability of nanoscale Mn-Ni-Si precipitates formed at lower temperature in highly irradiated reactor pressure vessel steels, Sci. Rep. 9 (1) (2019) 9587.
[30] G. Bonny, D. Terentyev, A. Bakaev, E.E. Zhurkin, M. Hou, D. Van Neck, L. Malerba, On the thermal stability of late blooming phases in reactor pressure vessel steels: an atomistic study, J. Nucl. Mater. 442 (1–3) (2013) 282–291.
[31] N. Castin, G. Bonny, A. Bakaev, F. Bergner, C. Domain, J.M. Hyde, L. Messina, B. Radiguet, L. Malerba, The dominant mechanisms for the formation of solute-rich clusters in low-Cu steels under irradiation, Mater. Today Energy 17 (2020).
[32] N. Castin, G. Bonny, M.J. Konstantinović, A. Bakaev, F. Bergner, C. Courilleau, C. Domain, B. Gómez-Ferrer, J.M. Hyde, L. Messina, G. Monnet, M.I. Pascuet, B. Radiguet, M. Serrano, L. Malerba, Multiscale modelling in nuclear ferritic steels: from nano-sized defects to embrittlement, Mater. Today Phys. 27 (2022) 100802.
[33] P. Efsing, P. Ekström, Swedish RPV surveillance programs, in: W.L. Server, M. Brumovský (Eds.), International Review of Nuclear Reactor Pressure Vessel Surveillance Programs, ASTM International, West Conshohocken, PA, 2018, pp. 219–231.
[34] P. Efsing, C. Jansson, T. Mager, G. Embring, Analysis of the ductile-to-brittle transition temperature shift in a commercial power plant with high nickel containing weld material, in: J.T. Busby (Ed.), Effects of Radiation on Materials: 23rd International Symposium, ASTM International, West Conshohocken, PA, 2008, pp. 44–55.
[35] P. Efsing, M. Boåsen, D. Klein, P. Arffman, N. Hytönen, S. Lindqvist, M. Thuvander, K. Lindgren, J. Roudén, Barsebäck as a research and development platform, extraction and analysis of service-aged and irradiated reactor pressure vessel material, Roskilde, 2022.
[36] N. Hytönen, Z. Que, P. Arffman, J. Lydman, P. Nevasmaa, U. Ehrnstén, P. Efsing, Effect of weld microstructure on brittle fracture initiation in the thermally- aged boiling water reactor pressure vessel head weld metal, Int. J. Miner., Metall. Mater. 28 (5) (2021) 867.
[37] S. Lindqvist, A. Norrgård, P. Arffman, N. Hytönen, J. Lydman, P. Efsing, S. Suman, P. Nevasmaa, Mechanical behavior of high-Ni/high-Mn Barsebäck 2 reactor pressure vessel welds after 28 years of operation, J. Nucl. Mater. 581 (2023) 154447.
[38] K. Lindgren, P. Efsing, M. Thuvander, Elemental distribution in a decommissioned high Ni and Mn reactor pressure vessel weld metal from a boiling water reactor, Nucl. Mater. Energy 36 (2023).
[39] H. Yuya, K. Yabuuchi, A. Kimura, Radiation embrittlement of clad-HAZ of RPV of a decommissioned BWR plant, J. Nucl. Mater. 557 (2021).
[40] K. Thompson, D. Lawrence, D.J. Larson, J.D. Olson, T.F. Kelly, B. Gorman, In situ site-specific specimen preparation for atom probe tomography, Ultramicroscopy. 107 (2–3) (2007) 131–139.
[41] J.M. Hyde, M.G. Burke, B. Gault, D.W. Saxey, P. Styman, K.B. Wilford, T. J. Williams, Atom probe tomography of reactor pressure vessel steels: an analysis of data integrity, Ultramicroscopy. 111 (6) (2011) 676–682.
[42] B. Gault, M.P. Moody, F. de Geuser, G. Tsafnat, A. La Fontaine, L.T. Stephenson, D. Haley, S.P. Ringer, Advances in the calibration of atom probe tomographic reconstruction, J. Appl. Phys. 105 (3) (2009).
[43] A.J. Breen, A.C. Day, B. Lim, W.J. Davids, S.P. Ringer, Revealing latent pole and zone line information in atom probe detector maps using crystallographically correlated metrics, Ultramicroscopy. 243 (2023) 113640.
[44] J.M. Hyde, A. Cerezo, T.J. Williams, Statistical analysis of atom probe data: detecting the early stages of solute clustering and/or co-segregation, Ultramicroscopy. 109 (5) (2009) 502–509.
[45] F. De Geuser, B. Gault, Metrology of small particles and solute clusters by atom probe tomography, Acta Mater. 188 (2020) 406–415.
[46] B.M. Jenkins, A. Zakirov, F. Vurpillot, A. Etienne, C. Pareige, P. Pareige, B. Radiguet, On the iron content of Mn-Ni-Si-rich clusters that form in reactor pressure vessel steels during exposure to neutron irradiation, Acta Mater. 281 (2024).
[47] Y. Dong, A. Etienne, A. Frolov, S. Fedotova, K. Fujii, K. Fukuya, C. Hatzoglou, E. Kuleshova, K. Lindgren, A. London, A. Lopez, S. Lozano-Perez, Y. Miyahara, Y. Nagai, K. Nishida, B. Radiguet, D.K. Schreiber, N. Soneda, M. Thuvander, T. Toyama, J. Wang, F. Sefta, P. Chou, E.A. Marquis, Atom probe tomography interlaboratory study on clustering analysis in experimental data using the

maximum separation distance approach, Microsc. Microanal.: Off. J. Microsc. Soc. America, Microbeam Anal. Soc., Microscop. Soc. Canada 25 (2) (2019) 356–366.
[48] N. Castin, P. Klupś, M. Konstantinovic, G. Bonny, M.I. Pascuet, M. Moody, L. Malerba, How precisely are solute clusters in RPV steels characterized by atom probe experiments? J. Nucl. Mater. (2024) 155412.
[49] K. Murakami, Influence of copper precipitates on clustering behavior of alloying elements observed in Japanese reactor pressure vessel surveillance materials using atom probe tomography, J. Nucl. Mater. 542 (2020).
[50] Y. Sekio, S. Yamashita, N. Sakaguchi, H. Takahashi, Void denuded zone formation for Fe–15Cr–15Ni steel and PNC316 stainless steel under neutron and electron irradiations, J. Nucl. Mater. 458 (2015) 355–360.
[51] B.N. Singh, Effect of grain size on void formation during high-energy electron irradiation of austenitic stainless steel, Philos. Mag.: J. Theoret. Exp. Appl. Phys. 29 (1) (1974) 25–42.
[52] K. Lindgren, M. Boåsen, K. Stiller, P. Efsing, M. Thuvander, Cluster formation in in-service thermally aged pressurizer welds, J. Nucl. Mater. 504 (2018) 23–28.
[53] K. Lindgren, M. Boåsen, Z. Que, K. Stiller, P. Efsing, M. Thuvander, Post-irradiation annealing of high flux irradiated and surveillance material reactor pressure vessel weld metal, J. Nucl. Mater. 562 (2022).
[54] N. Almirall, P.B. Wells, S. Pal, P.D. Edmondson, T. Yamamoto, K. Murakami, G. R. Odette, The mechanistic implications of the high temperature, long time thermal stability of nanoscale Mn-Ni-Si precipitates in irradiated reactor pressure vessel steels, Scr. Mater. 181 (2020) 134–139.
[55] B.M. Jenkins, P.D. Styman, N. Riddle, P.A.J. Bagot, M.P. Moody, G.D.W. Smith, J. M. Hyde, Observation of Mn-Ni-Si-rich features in thermally-aged model reactor pressure vessel steels, Scr. Mater. 191 (2021) 126–130.